J. Fluid Mech. (1989), *vol.* 200, *pp.* 149–171
Printed in Great Britain

On flow separation and reattachment around a circular cylinder at critical Reynolds numbers

By H. HIGUCHI†, H. J. KIM‡ AND C. FARELL†

†St Anthony Falls Hydraulic Laboratory, Department of Civil & Mineral Engineering, University of Minnesota, Minneapolis, MN 55414, USA

‡Korea Advanced Institute of Science and Technology, Seoul, Korea

(Received 18 September 1987 and in revised form 14 June 1988)

An experimental investigation of the flow around smooth circular cylinders in the Reynolds number range $0.8 \times 10^5 < Re < 2 \times 10^5$ is presented. Measured quantities include spectra, spanwise correlations and cross correlations of cylinder pressures and wake-velocity fluctuations, and low-frequency boundary-layer flow direction reversals near separation. The flow motion in the critical range is found to be characterized by intermittent, symmetric boundary-layer reattachments, occurring in cells with a well-defined spanwise structure, accompanying a significant decrease in drag coefficient and a weakening of the vortex shedding.

1. Introduction

The transition separating the subcritical and supercritical regimes of circular cylinder flows is marked by a pronounced decrease in the drag coefficient, C_d, from about 1.15 at $Re \approx 1.5 \times 10^5$, to about 0.25 at $Re \approx 4 \times 10^5$ (see figure 1). Actual values vary for different experimental set-ups, since flow characteristics in the transition range are rather sensitive to parameters such as surface roughness, wind tunnel wall interference, oncoming stream turbulence, end boundary conditions, and cylinder aspect ratio. This range of pronounced decrease in C_d is referred to herein as the critical Reynolds number range. It is now accepted (Bearman 1969; Farell & Blessman 1983) that the formation of laminar separation–turbulent reattachement bubbles on both sides of the cylinder is responsible for the low values of C_d which occur at the beginning of the supercritial regime. Existing measurements, however, do not yet provide a complete understanding of the mechanics of the boundary-layer reattachment on both sides of the cylinder, in particular in regard to the possible occurrence of three-dimensional spanwise structures (Humphreys 1960; Korotkin 1976) in or near the critical transition, under closely two-dimensional boundary conditions.

Two subregions have been distinguished in the critical transition (Farell & Blessman 1983; also Almosnino & McAlister 1984). The first is characterized by symmetric mean pressure distributions (time averaged relative to the vortex shedding period) and by a gradual decrease in C_d and vortex shedding intensity as Re increases, accompanied by increasing non-uniformity along the cylinder span. In the second subregion intense flow oscillations occur, with typical timescales much larger than the vortex shedding period, which are associated with unsteady asymmetric reattachment of the cylinder boundary layers without preference for side. Asymmetric, quasi-steady, multivalued pressure distributions result, involving substantial lift forces. Velocity and pressure fluctuation spectra appear in general

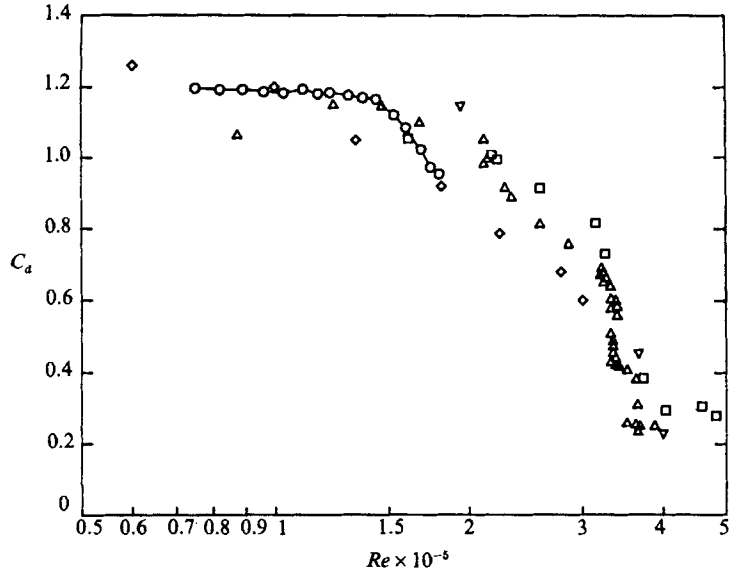

FIGURE 1. Drag coefficient as a function of Reynolds number (corrected for blockage). ○, present results (model A); △, Farell & Blessman (1983); □, Güven, Farell & Patel (1980); ◇, Achenbach (1968); ▽, Bearman (1969).

with broad band peaks as shedding under different oscillating flow configurations adds succeeding spectral components with different Strouhal numbers.

The present investigation was specifically directed at the study of the flow in the first subregion, aiming at characterizing the mechanics of the reattachment process and the decrease in C_d in this range. The large-time scale dependence of the vortex shedding and the associated boundary-layer motions were investigated, with particular attention paid to the spanwise structure of the flow. A description of the experiments, instrumentation, and procedure is presented in §2. The experimental results, which include mean pressures, pressure and velocity fluctuations, spanwise correlations and cross correlations between pressures and velocities, and boundary-layer flow direction measurements near separation, are summarized in §3. Section 4 presents a discussion of results, and §5 a summary of conclusions.

2. Description of the experiment

2.1. *Wind tunnel and models*

The experiment was conducted using two circular cylinder models spanning the test section of a low-speed, open-return wind tunnel. The test section is 30.5 cm wide, 43.2 cm high, and 1.83 m long, and has tapered sidewalls to give constant static pressure along the tunnel axis. At the maximum tunnel speed of about 70 m/s, the free-stream turbulence intensity was about 0.3%; the turbulence intensity was higher at low tunnel speeds, about 0.6% at 10 m/s, the lowest speed used in the present study. Variations in mean flow velocity, U, outside the tunnel boundary layers were less than 1%. Figure 2 shows representative free-stream mean and fluctuating velocity distributions in the vertical (y) direction at near maximum

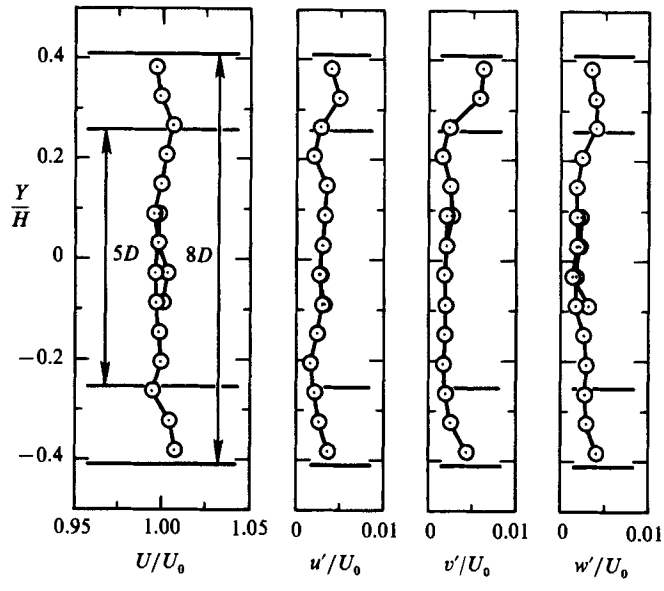

FIGURE 2. Free-stream mean and fluctuating velocity distributions in the vertical (y) direction at near maximum tunnel speeds. Lines at $8D$ and $5D$ spacings indicate locations of end plates.

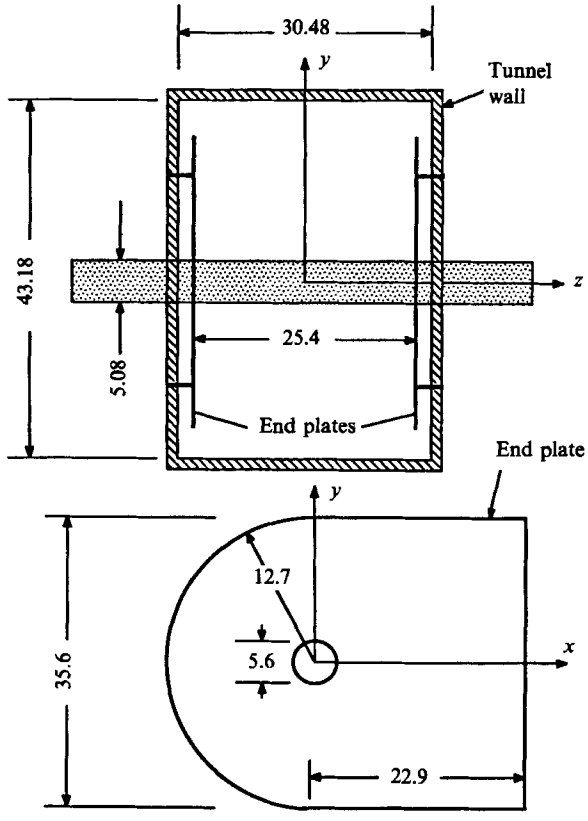

FIGURE 3. Cylinder model A with end plates in the wind tunnel (all dimensions in cm).

tunnel speeds. The location of the end plates is also shown in the figure. A more detailed description of free-stream conditions can be found in Kim (1986).

The cylinder models tested had diameters of 5.08 cm (model A) and 4.42 cm (model B), and aspect ratios respectively of 5 and 8. Model A was placed horizontally at mid-height in the test section (see figure 3) 30 cm downstream from the end of the contraction, resulting in a blockage ratio of 11.8%. Model B was installed vertically at mid-width in the test section, 132 cm downstream from the test section inlet, resulting in a blockage ratio of 13.9%. Each model was provided with end plates. For model A, the end plates were the same as used by Farell and Fedeniuk (1987) and were fixed at 2.54 cm from the tunnel sidewalls, giving an aspect ratio of 5. The end plates of model B were circular, with a diameter of 30.5 cm, and were made movable so that the aspect ratio could be changed. The maximum aspect ratio was $AR = 8$ (end plates 3.9 cm away from the tunnel floor and ceiling). Each model was supported outside the test section to eliminate any transmission of tunnel vibrations. The small gaps between the models and the tunnel walls were sealed with silicon rubber or adhesive tape. The model surfaces were given a smooth finish using fine emery cloth; the relative surface roughnesses were estimated to be of the order of 10^{-5}.

2.2. *Instrumentation and experimental procedure*

Pressure taps were provided on model A at three spanwise positions. The main measuring section at $z/D = 0.3$ contained 30 taps, drilled at 10° intervals for angles $\theta < 120°$ (θ = circumferential angle measured from the forward stagnation point) and at 20° intervals otherwise. Cartesian coordinates are defined here with the z-axis in the spanwise direction, the x-axis is the streamwise direction, and the origin at mid-span on the cylinder axis (see figure 3). A few additional taps were available at $z/D = 1.7$ and $z/D = -1.3$. The tap opening diameter was 0.8 mm. The pressure taps were connected, via 0.8 mm internal diameter plastic tubings, to a scanning valve connected to a pressure transducer. Several capacitance-type pressure transducers were used, depending on the pressure levels. Calibration of the time response of this system showed that, if the taps were connected directly to the sensors via short tubings, they could be used to measure low-frequency fluctuations of the order of a few Hertz without significant phase shift. For measurements of high-frequency pressure fluctuations, a miniature pressure transducer 2.4 mm in diameter (Endevco 8507−2) was flush mounted on cylinder A at $\theta = 65°$ and $z/D = 0.45$. Velocity fluctuations and their spanwise correlations in the wake of model A were measured by single hot-wire probes and a two channel TSI 1050 constant-temperature anemometer.

Model B had 29 taps along a cylinder generatrix, at 1.27 cm intervals, installed by embedding 40 cm long, 0.8 mm internal diameter, metal tubings inside the cylinder body. One pressure tap was provided on the opposite side of the model at mid-span. These taps were used for measurement of low-frequency pressure fluctuations (in addition to mean pressures) by connecting them to additional Endevco 8507−2 pressure transducers. In addition to the pressure taps, an instantaneous flow direction sensor was later installed on the surface of model B at $z/D = -0.15$, on the same generatrix as the taps. This probe is a surface fence probe, being developed as a modified version of an earlier probe (Higuchi 1985), and consisting of two pressure transducers and a small fence between them. For the present application, both for simplicity and to keep the probe size small, external pressure transducers (Endevco 8507−2) were connected to 0.4 mm surface taps by 40 cm long, 0.4 mm internal diameter tubings. The fence was 1.27 mm long and 0.4 mm high. The time-dependent

flow direction at the probe location was determined by monitoring the instantaneous pressure difference between the two probe taps. The limitations of this sensor and possible effect on the flow are discussed later.

The fluctuating pressure signals of the pressure tap–pressure transducer combinations (without the scanning valve) and of the flow-direction detector were low-pass filtered at 20 Hz. This frequency was below the response frequencies of the systems. Real time traces of pressures and velocities were obtained with a Nicolet 4094 four-channel digital oscilloscope, and data acquisition and reduction were performed on a HP 9836 microcomputer. In addition to using an FFT algorithm on the microcomputer, an HP 3582A dual channel spectrum analyser was also used for speed and convenience to obtain spectral density functions and cross spectra. For additional details regarding the instrumentation and experimental procedure, reference is made to Kim (1986).

3. Experimental results

3.1. *Mean pressure measurements*

Figure 4 shows circumferential pressure distributions obtained with model B at $Re = 1.95 \times 10^5$. Substantial spanwise changes in the minimum pressure coefficients, C_{pm}, can be observed. The base pressure coefficients, C_{pb}, on the other hand, remain constant along the span, and this results in relatively small changes in the C_d values (see figure inset). These measurements on model B were made by rotating the cylinder to change the angular position of the generatrix containing the pressure taps, a valid procedure because of the 'steadiness' of the flow as observed with both cylinder models in the Reynolds-number range investigated, which corresponds to the first of the two critical subregions identified in §1. The range investigated is illustrated in figure 1, which shows C_d data obtained on model A (corrected for blockage according to the method by Allen & Vincenti 1944) together with limited data from other studies. Comparison with these data is not pursued in any detail because no data from these other studies are available regarding the spanwise variations documented herein, and also because of the sensitivity of the flow in the range in question to parameters such as surface roughness, wind tunnel wall interference, oncoming stream turbulence, end boundary conditions, and cylinder aspect ratio. The measured C_{pb} on model A generally agreed, both in value and trend, with other available data. Small differences with the results of model A were observed in the C_{pb} and C_d values measured on model B, but these were not investigated further for the reasons outlined.

Mean pressure maps obtained for subcritical and critical Re by rotating model B as discussed above are presented in figures 5, 6, and 7. No attempt has been made at introducing a blockage correction, which would be qualitative at best. A well-defined cellular pattern can be seen in the pressure map of figure 6 for $AR = 8$ and a critical $Re = 1.95 \times 10^5$, in the region of minimum pressures between $\theta = 60°$ and $\theta = 90°$. Such a pattern is not present in the pressure map of figure 5 for a subcritical $Re = 1.02 \times 10^5$, which shows only a small dip in pressure near the mid-span in this region. The cell-type structures can also be seen in the map of figure 7 for critical Re and $AR = 5$, which shows some effect of the smaller cylinder length.

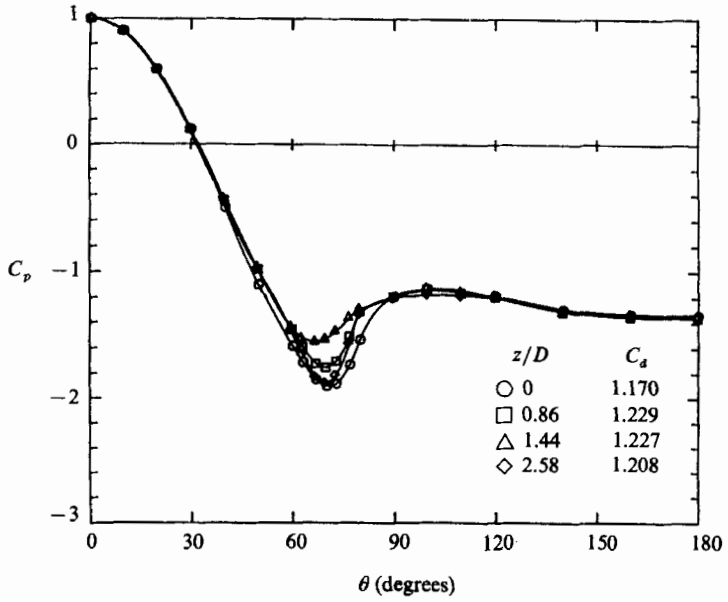

FIGURE 4. Circumferential pressure distributions (not corrected for blockage) at $Re = 1.9 \times 10^5$ and $AR = 8$.

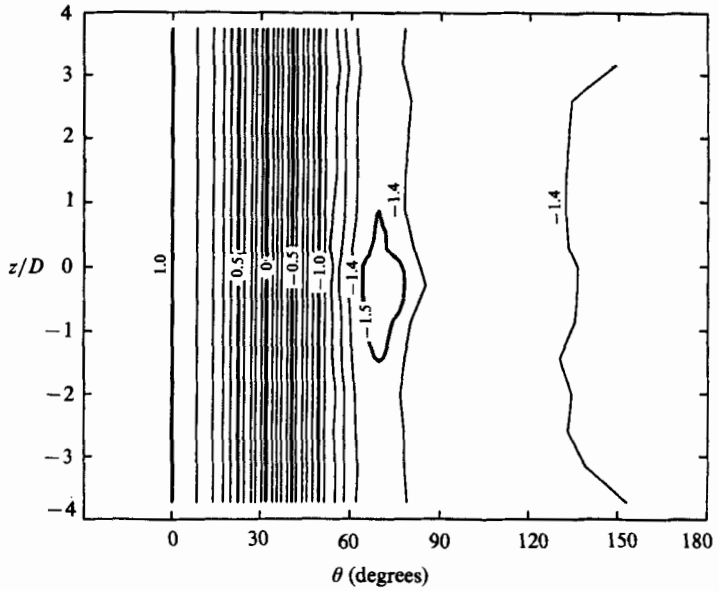

FIGURE 5. Constant pressure contours at $Re = 1.02 \times 10^5$ and $AR = 8$.

3.2. *Pressure and velocity fluctuation measurements*

3.2.1. *Spectral measurements*

Pressure fluctuation spectra at $\theta = 65°$ and $z/D = 0.45$ are presented in figure 8 for the range of Re investigated. Wake velocity spectra were also obtained but are not presented here for brevity, the only difference with the spectra of figure 8 being somewhat smaller energy levels in the velocity spectra at low frequencies. The peak

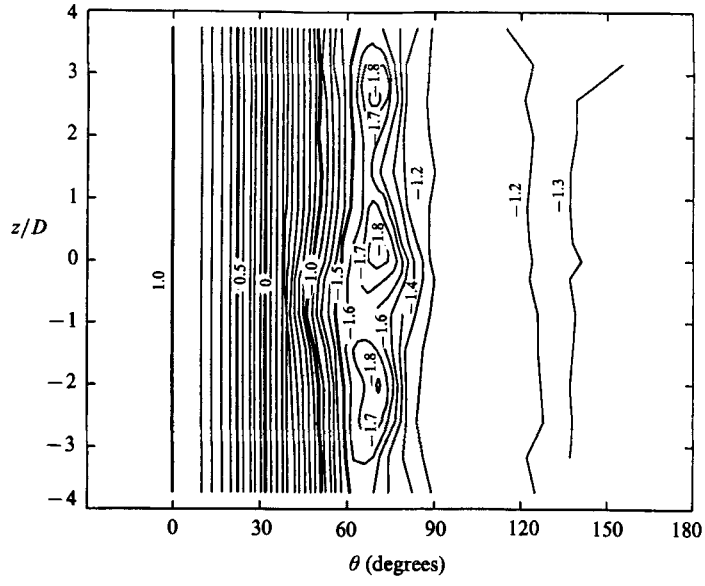

FIGURE 6. Constant pressure contours at $Re = 1.95 \times 10^5$ and $AR = 8$.

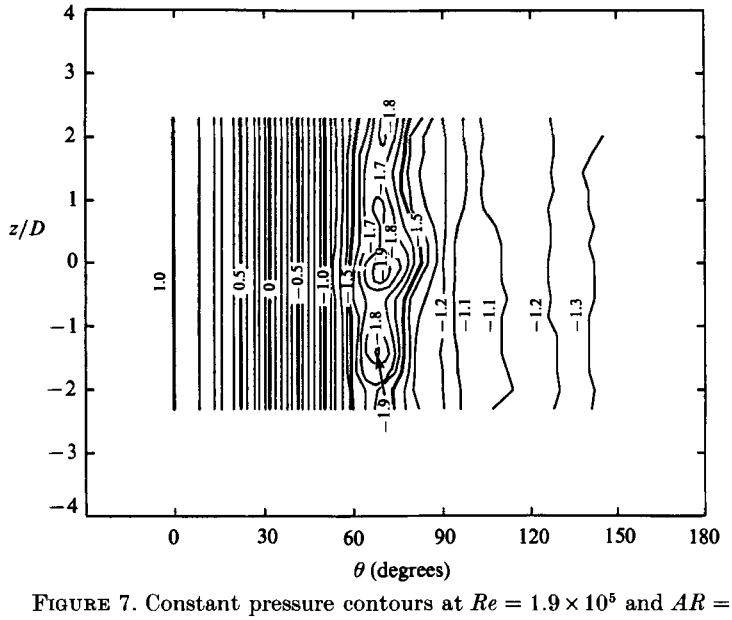

FIGURE 7. Constant pressure contours at $Re = 1.9 \times 10^5$ and $AR = 5$.

Strouhal numbers were fairly constant and in general agreement with other published data (see preceding discussion in §3.1). As seen in figure 8, the intensity of the shedding decreased markedly as Re increased beyond about 1.5×10^5. This decrease was accompanied by a broadening of the peaks and also by a shift in energy toward low-frequency components. These findings corroborate those of Schewe (1983) and Farell & Blessman (1983).

To investigate further these low-frequency components, the coherence function between the cylinder pressure fluctuations (at $\theta = 65°$ and $z/D = 0.45$) and the wake

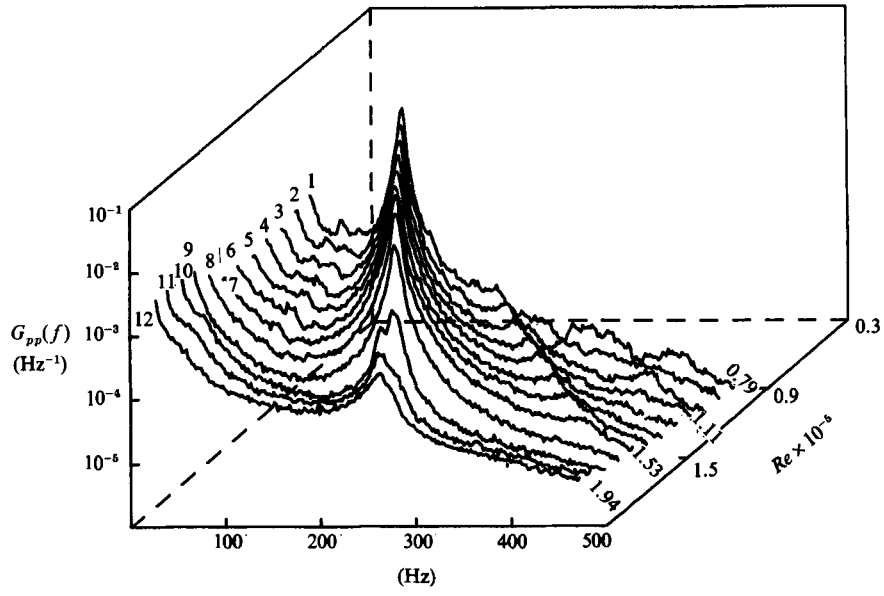

FIGURE 8. Surface pressure spectra (normalized by the free-stream dynamic pressure).

No.	1	2	3	4	5	6	7	8	9	10	11	12
$Re \times 10^{-5}$	0.79	0.90	1.00	1.11	1.22	1.33	1.44	1.54	1.65	1.75	1.85	1.94

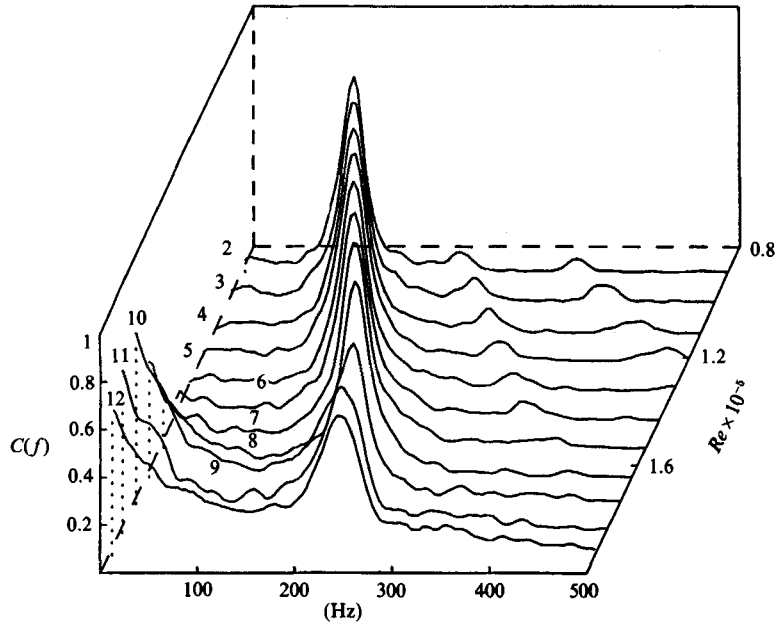

FIGURE 9. Coherence between surface pressure and wake velocity fluctuations.

No.	1	2	3	4	5	6	7	8	9	10	11	12
$Re \times 10^{-5}$	0.79	0.90	1.00	1.11	1.22	1.33	1.44	1.54	1.65	1.75	1.85	1.94

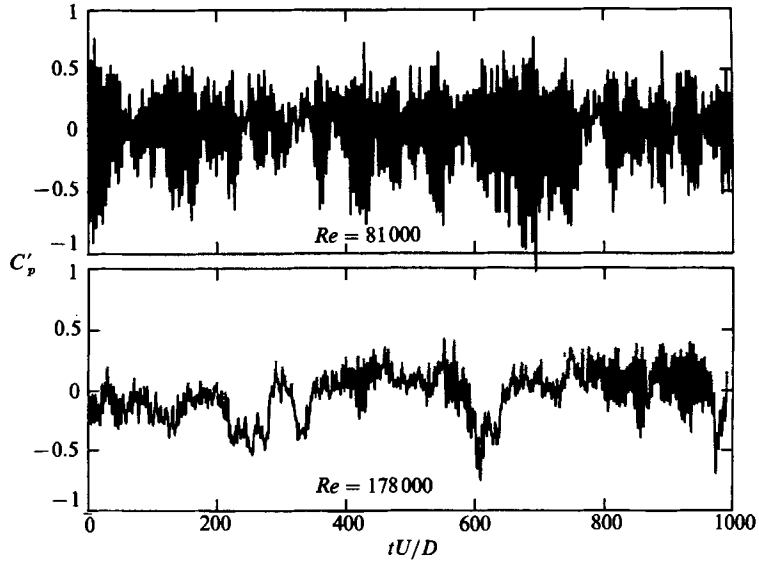

FIGURE 10. Pressure–time traces at $\theta = 65°$, $z/D = 0.45$ for $Re = 0.81 \times 10^5$ ($U/D = 493$ s^{-1}) and $Re = 1.78 \times 10^5$ ($U/D = 1083$ s^{-1}).

velocity fluctuations (at $z/D = 0.45$, $x/D = 1.45$, and $y/D = 0.5$) was measured and is presented in figure 9. While in the subcritical range high coherence values were found only in the neighbourhood of the vortex shedding frequency, figure 9 shows that for $Re > 1.5 \times 10^5$ relatively high values were obtained also at low frequencies, pointing to coherent flow motions at these frequencies. The occurrence of higher harmonics of the vortex shedding frequency can be observed in both figures 8 and 9.

3.2.2. *Pressure–time traces*

Figure 10 shows pressure–time traces measured with the flush-mounted transducer at $\theta = 65°$ and $z/D = 0.45$ for two Reynolds numbers: subcritical ($Re = 0.81 \times 10^5$) and critical ($Re = 1.78 \times 10^5$). The sampling time was 0.5 ms. In the subcritical case, regular oscillations associated with the vortex shedding frequencies can be observed, with the amplitude modulations similar to those described by Sonneville (1976). For the larger, critical Re, large-timescale variations were observed, associated with suppression of the regular vortex shedding, and involving pressure excursions always toward more negative values.

3.2.3. *Cross-correlations between filtered velocity and pressure signals*

For investigation of the low-frequency components of the motion, the velocity and pressure data for $Re = 1.88 \times 10^5$, sampled at 0.5 ms intervals, were numerically low-pass filtered by calculating moving averages over 20 ms time periods. The location of the pressure transducer was $\theta = 65°$, $z/D = 0.45$; the single hot-wire probe was located directly downstream from it, at $x/D = 0.2$, $y/D = 0.5$, $z/D = 0.45$. Figure 11 shows the low-pass filtered pressure and velocity traces for $Re = 1.88 \times 10^5$, together with their instantaneous cross-correlation product (the integrand of the cross correlation between them).

The large negative values of the cross-correlation product in figure 11 correspond to the large-timescale variations and suppression of regular vortex shedding

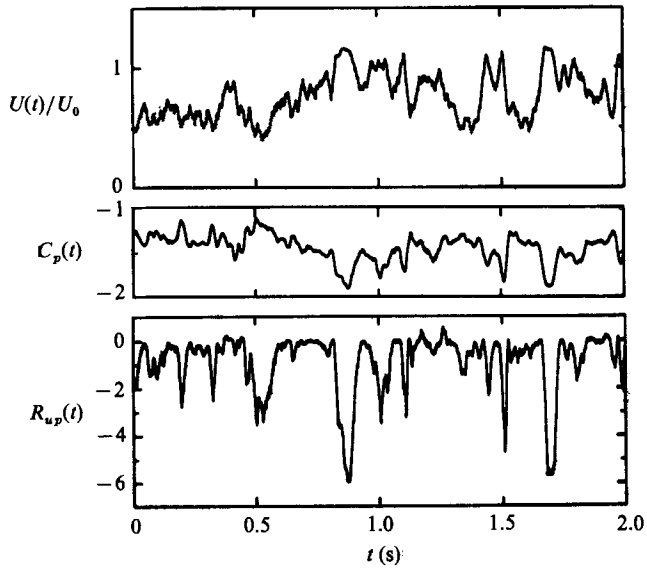

FIGURE 11. Low-pass filtered velocity and pressure traces and their instantaneous product for $Re = 1.88 \times 10^5$.

observed in the pressure traces. The magnitude of the velocity signal increased in unison with the negative pressure excursions. The velocity variations were large (in the range from, say, 0.2 U_0 to 1.3 U_0) suggesting random, slow motions of the wake boundary, with the hot-wire probe moving into and out of the wake. Although the accuracy of the velocity measurements is suspect inside the wake region, the effect is not significant for the purpose of the present measurements.

3.3. *Time-dependent boundary layer separation*

3.3.1. *Cross-correlation between pressures at symmetric locations on the cylinder*

For further study of the large-timescale, large-amplitude pressure fluctuations observed at critical Re, low-frequency pressure fluctuations were measured simultaneously at $\theta = 90°$ and $\theta = -90°$, at mid-span of model B, low-pass filtered at 20 Hz, and cross-correlated. As shown in figure 12 for $Re = 1.92 \times 10^5$, the low-frequency fluctuations were highly correlated, indicating symmetric and in-phase flow components. Similar symmetric and in-phase low-frequency fluctuations were detected at subcritical Re. Time-averaged circumferential cross-correlations between low-frequency pressure fluctuations at various azimuthal distances were also measured, using the pressure taps on model A. These measurements showed that the low-frequency fluctuations were equally well correlated at both subcritical and critical Re, except for somewhat lower correlations (about 0.4) at critical Re involving points within the wake region.

3.3.2. *Instantaneous flow-direction measurements*

In order to diagnose the low-frequency movements of the boundary layer on the cylinder, the flow-direction sensor described in §2.2 was installed later on model B (at $z/D = -0.15$), and instantaneous pressure differences across the fence were obtained at different angular positions and low-pass filtered at 20 Hz. Unlike in earlier surface

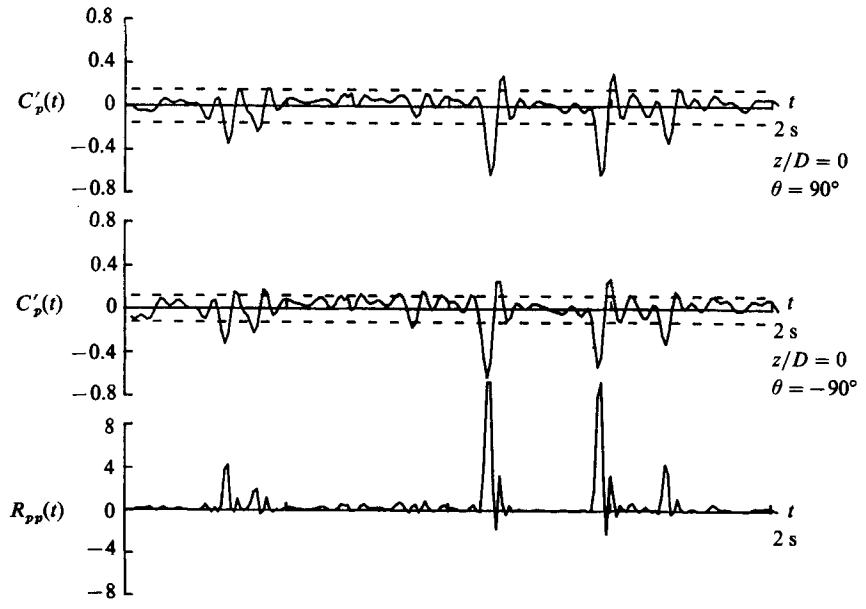

FIGURE 12. Low-pass filtered pressure traces at symmetric points on the cylinder and their cross-correlation product $R_{pp}(t)$, for $Re = 1.93 \times 10^5$ (dotted lines, r.m.s. values).

fence probes (e.g. Achenbach 1968; Higuchi 1985), the relative size of the present fence element was a substantial fraction of the boundary-layer thickness, due partly to the sensitivity of the available dynamic pressure transducer. The transducer output thus represented an average over a relatively large fence height, and no attempt was made to convert this output to absolute values of velocity or shear stress. Rather, the transducer signal was used to detect flow direction: a zero differential pressure reading of the sensor was interpreted as a spatially averaged zero flow across the fence height. As for possible interference with the flow, the presence of the fence probe did not have any effect on the other measurements being conducted.

The frequency response of the system as implemented was limited to an order of magnitude smaller than the vortex shedding frequency. Boundary-layer oscillations with amplitudes of a few degrees are known to be induced by the vortex shedding (Dwyer & McCroskey 1973). Since these oscillations are not symmetric about the mean, their time averaging by the sensor is likely to cause some skewing of the present data. Skewing also results from the spatial averaging due to the finite fence height. In both cases it is expected that the skewing will shift the point of zero sensor differential pressure away from the point of zero skin friction and in the direction of the actual separation point of the unsteady boundary layer (see §4.1).

Subcritical pressure traces obtained with the fence sensor showed predominantly positive values at 84°, indicating flow in the streamwise direction. As the probe was moved downstream, the fence pressure differences became more frequently negative than positive at $\theta = 88°$. At $\theta = 90°$, the values were mostly negative. In other words, the chance of flow reversal increased with θ until the probe was entirely in the reversed flow region. In addition, the position of zero flow across the fence was found to be non-stationary, moving with timescales substantially larger than the vortex shedding period.

Figure 13 shows the differential pressure traces (low-pass filtered at 20 Hz) of the

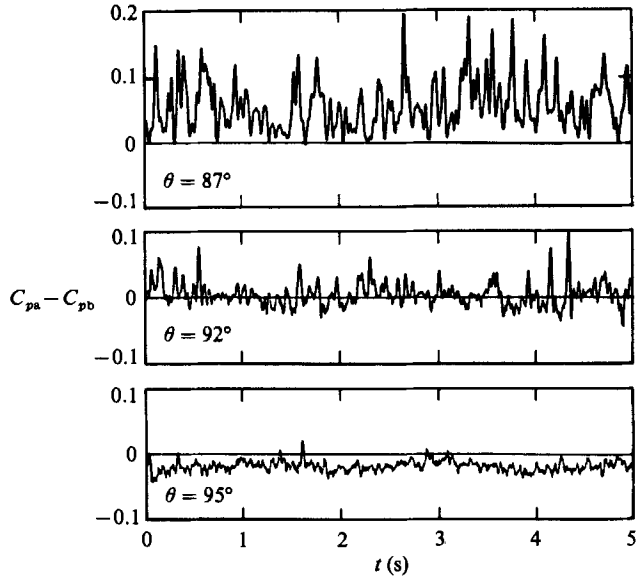

FIGURE 13. Fence probe differential pressure traces, $Re = 1.96 \times 10^5$.

fence probe for $Re = 1.96 \times 10^5$ at three angular positions At this critical Re, the fence pressure differences were predominantly positive at $\theta = 87°$. They became very small, indicating practically zero flow, near $\theta \approx 89°$ (trace not shown in figure 13). Further downstream ($\theta = 92°$), the pressure trace indicated intermittent flow in the downstream direction, suggesting that the separated flow upstream had reattached. Still further downstream ($\theta = 95°$) the pressure differences were practically always negative, indicating that the probe was within the final separated flow region, with low signal levels corresponding to the low values of the wake velocities.

Figure 14 shows the fraction of time, F_t, corresponding to flow in the downstream direction at various angular positions, computed from the differential time traces, at three Re. The parameter F_t decreases monotonically with increasing angle at subcritical Re ($Re = 1.59 \times 10^5$ was the approximate boundary between subcritical and critical flow in these experiments). For the critical $Re = 1.96 \times 10^5$, on the other hand, F_t decreases sharply first to practically zero, and then increases to a local maximum at $\theta \approx 92°$. Exactly the same results were obtained on the opposite side of the cylinder.

3.3.3. *Time-dependent vortex shedding*

The effect of the flow reattachment on the vortex shedding can be illustrated by taking conditionally sampled spectra in the critical range. Spectra averaged over long observation times showed weak and broadband spectral peaks at the shedding frequency (see figure 8). To examine the shedding under reattached and non-reattached flow conditions, the pressure–time traces (figure 10) were divided in a somewhat subjective manner into time segments with similar characteristics, which were grouped into three families. Family A segments exhibited regular vortex shedding oscillations about mean pressure levels corresponding to subcritical flow conditions with no reattachment. Family C segments corresponded to the large-time-scale excursions to much lower mean pressure levels, indicating flow reattachment.

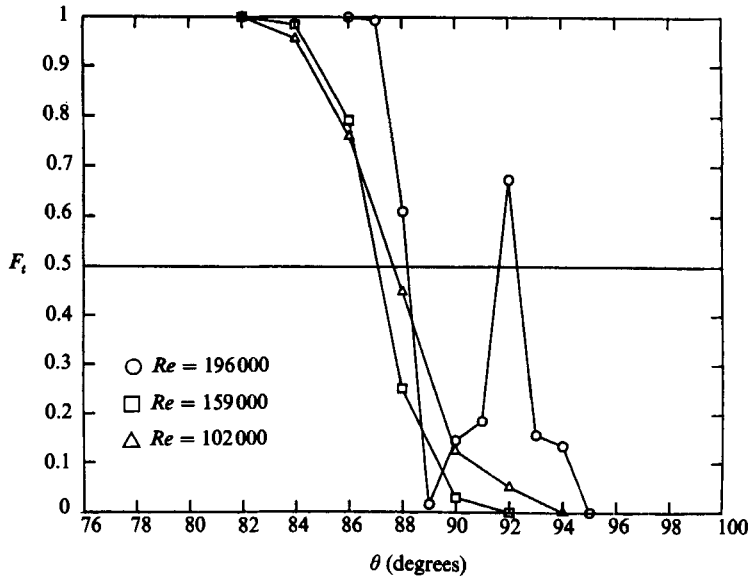

FIGURE 14. Fraction of time corresponding to flow in the downstream direction. ○, $Re = 1.96 \times 10^5$; □, $Re = 1.59 \times 10^5$; △, $Re = 1.02 \times 10^5$.

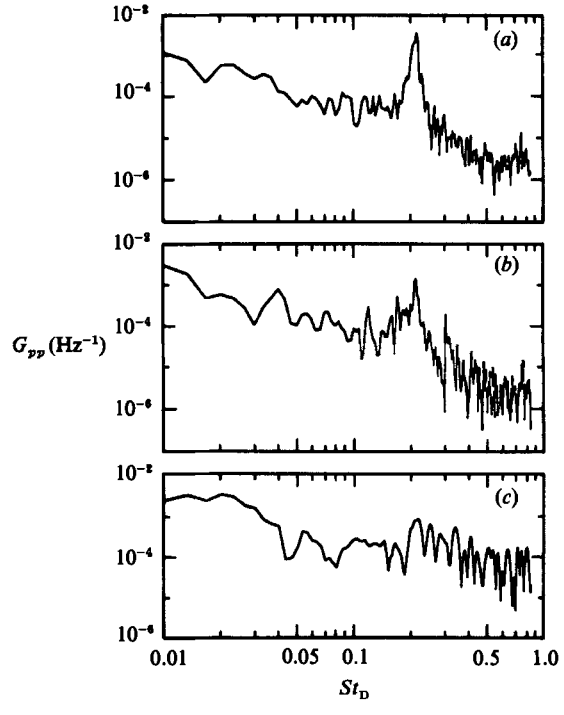

FIGURE 15. Ensemble averages of pressure spectra at $\theta = 65°$, $z/D = 0.45$ for time segments belonging to the same family. (*a*) family A; (*b*) family B; (*c*) family C. $Re = 1.78 \times 10^5$.

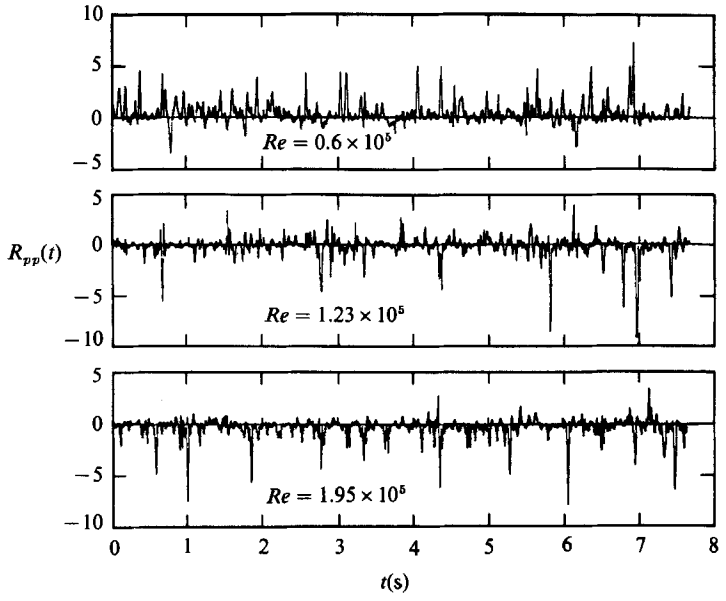

FIGURE 16. Instantaneous cross-correlation products of low-pass filtered pressure signals. Axial separation distance $\Delta z = 2.58D$, $\theta = 90°$.

Finally family B corresponded to shifts between family A and family C type segments.

Fast Fourier transform calculations were then performed on the individual time segments to obtain the corresponding spectra, and ensemble averages of the spectra of the same families were calculated. The results are shown in figure 15. When the flow was reattached at the spanwise location of figure 10 (family C), the vortex shedding was weak and merely discernible. On the other hand, relatively strong vortex shedding was observed when the flow remained detached (family A). For the time segments of family B, intermediate shedding states were found. Another distinct character of spectrum C was that, at low frequencies, it had considerably more energy than spectrum A, reflecting the effect of the large-timescale variations in the real time signal.

3.4. *Spanwise cross-correlation measurements*

3.4.1. *Time-dependent cross-correlation of pressure fluctuations*

The flow separation on the cylinder was found to be non-stationary with large timescale motions. In order to investigate the spanwise nature of these unsteady separation motions, instantaneous spanwise cross-correlation traces between low-pass filtered pressure fluctuations were obtained with the taps on model B placed at $\theta = 90°$ as follows. The signals from the pressure transducers connected to any two individual pressure taps were low-pass filtered at 20 Hz, and the normalized product of the two signals, here denoted by $R_{pp}(t)$, calculated and plotted. (The time average of this instantaneous cross-correlation trace equals the conventional cross-correlation.) Because of the relatively small velocity range examined, no attempt was made at changing the cut-off value of 20 Hz to have a fixed range of non-dimensional frequency. Figure 15 shows the instantaneous cross-correlation products for three Re, for a spanwise separation distance $\Delta z = 2.58\ D$.

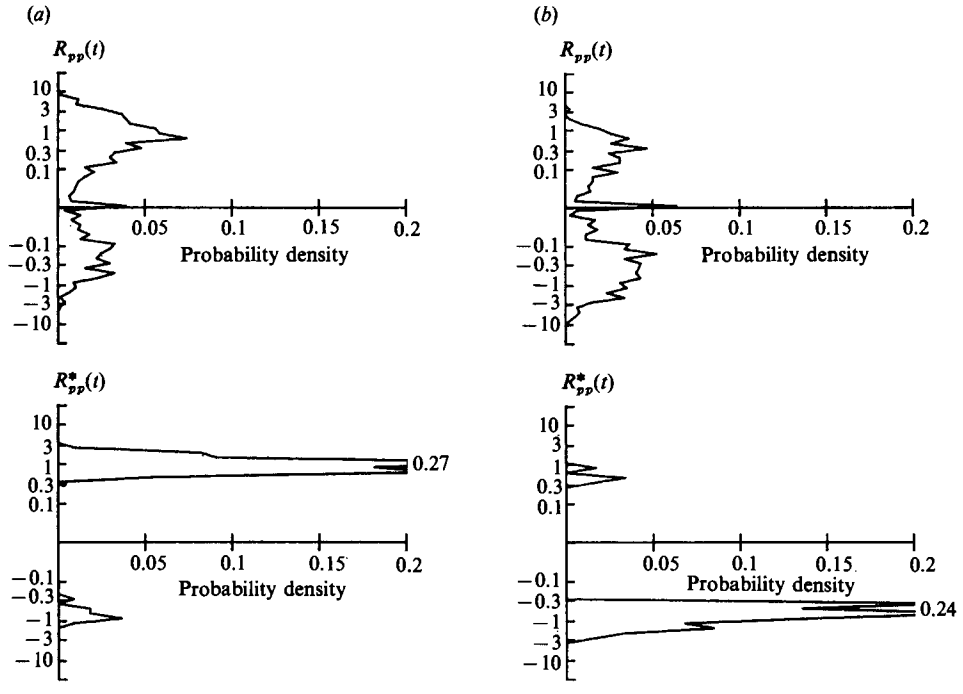

FIGURE 17. Probability density of instantaneous cross-correlation products for subcritical and critical Re. $R_{pp}(t)$ = unconditioned; $R^*_{pp}(t)$ = conditioned. (*a*) $Re = 0.6 \times 10^5$, $\Delta z/D = 2.58$. (*b*) $Re = 1.95 \times 10^5$, $\Delta z/D = 2.58$.

For the given spanwise positions of figure 16, positive products strongly predominated at subcritical Re. As Re increased, the instantaneous products began to exhibit more and more negative values. The contributions from the large negative peaks for $Re = 1.23 \times 10^5$ in figure 16 were just enough, as will be seen in figure 20, to make the conventional cross-correlation slightly negative. At $Re = 1.95 \times 10^5$, the product trace exhibited intermittent, high negative values. Calculation of the probability density function of the instantaneous cross-correlation products $R_{pp}(t)$ produced plots as shown in figure 17 (upper plots), exhibiting probability maxima at both positive and negative values of $R_{pp}(t)$. These maxima were different at subcritical and critical Re, and appeared to be largely due to the large-scale, large-amplitude pressure excursions. To highlight this point, the signals were conditioned by keeping only those time segments in which both signals exceeded their r.m.s. values (see e.g. figure 12). The corresponding signal product, here denoted by $R^*_{pp}(t)$, were then calculated. The probability density functions of the products $R^*_{pp}(t)$ so obtained are shown also in figure 17 (lower plots). At the critical $Re = 1.95 \times 10^5$ there is a large probability maximum at negative cross-correlation products. At the subcritical $Re = 0.6 \times 10^5$, on the other hand, the maximum occurs at positive cross-correlation products.

3.4.2. *Time-averaged spanwise pressure cross-correlations*

The spanwise distribution of the time-averaged cross-correlation between the low-frequency pressure fluctuations, unconditioned and conditioned as described in the preceding paragraph, are shown in figure 18 for $Re = 1.95 \times 10^5$ and $AR = 8$. (These are the time integrals of the functions $R_{pp}(t)$ and $R^*_{pp}(t)$ just defined.) The reference

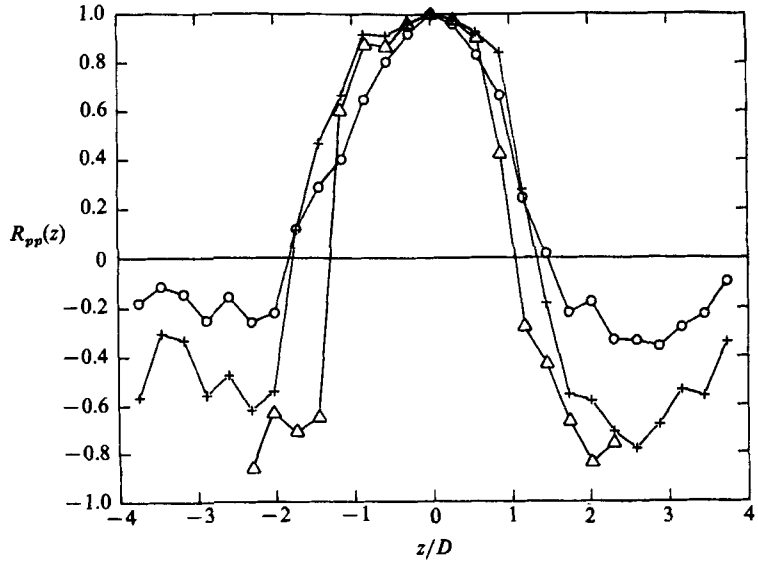

FIGURE 18. Spanwise variation of pressure cross-correlation coefficients (model B). $Re = 1.95 \times 10^5$, $AR = 8$; $Re = 2.0 \times 10^5$, $AR = 5$. Reference tap position at mid-span. Unconditioned: ○, $AR = 8$. Conditioned: +, $AR = 8$; △, $AR = 5$.

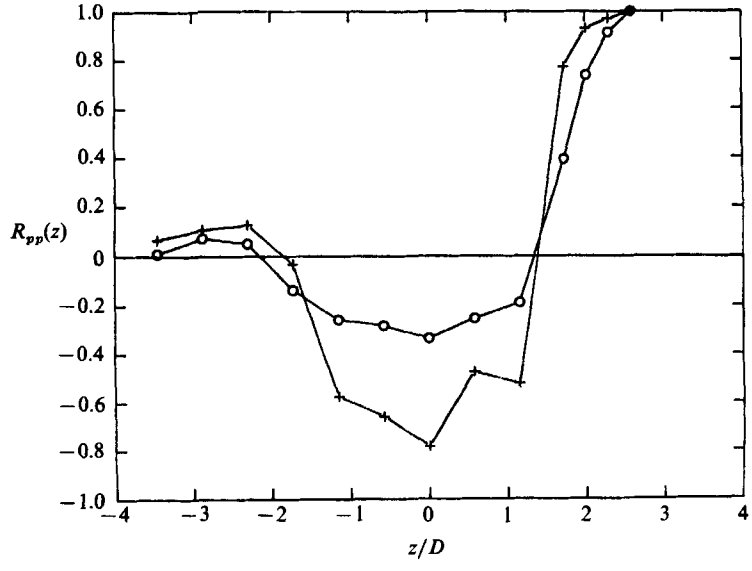

FIGURE 19. Spanwise variation of pressure cross-correlation coefficients (model B). $Re = 1.95 \times 10^5$, $AR = 8$, reference tap position at $z/D = 2.58$. ○, unconditioned; +, conditioned.

tap position was fixed at mid-span and $\theta = 90°$. While at subcritical Re the cross-correlation decreased monotonically with increasing spanwise distance, at the critical Re of the figure the cross-correlation exhibits a clear spanwise periodic pattern. Such periodic pattern was exhibited by all spanwise cross-correlations measured at Re larger than, say, 1.6×10^5. The measurements of figure 18 were repeated with a different reference tap position at $z/D = 2.58$, with essentially the same results, as shown in figure 19. They were also repeated with the same cylinder model (model B)

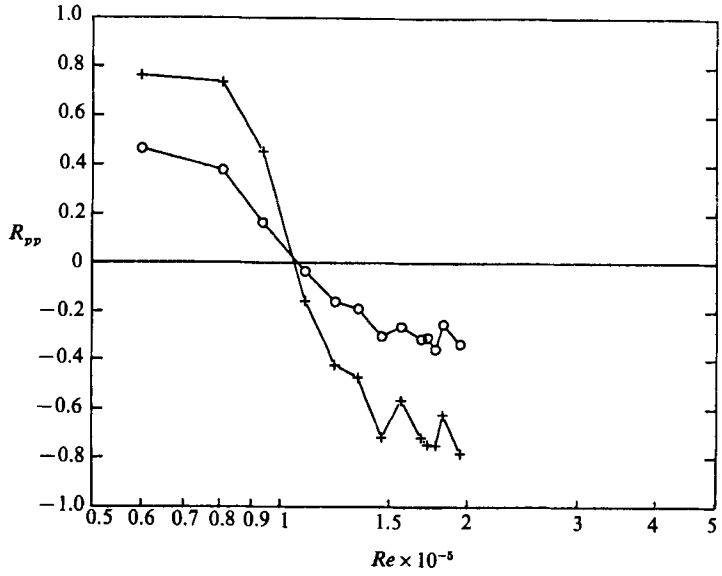

FIGURE 20. Variation of pressure cross-correlation coefficient with Re. Axial separation distance $\Delta z = 2.58\ D$, one tap at midspan. ○, Unconditioned; +, conditioned.

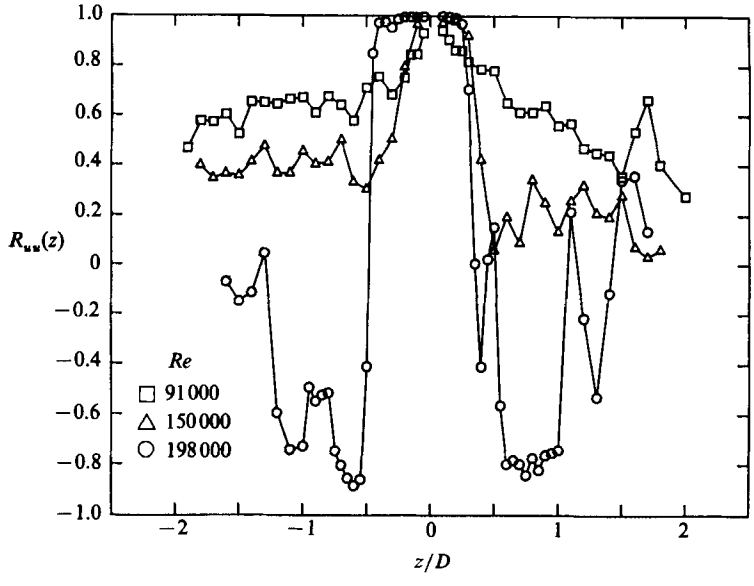

FIGURE 21. Spanwise variation of velocity cross-correlation coefficient at 3 Re (model A, $AR = 5$).

and $AR = 5$. A similar cell pattern with comparable cell size was obtained and is shown also in figure 18. The cross-correlation coefficient for $\Delta z/D = 2.58$ decreased monotonically with increasing Re as shown in figure 20.

3.4.3. *Time-averaged spanwise velocity cross-correlations*

These were measured in the wake of model A ($AR = 5$), with the reference hot-wire probe at $z/D = 0$ (mid-span), $x/D = 0.2$, and $y/D = 0.5$. The spanwise cross-correlations of the low-pass filtered at 2 Hz velocity fluctuations are shown in figure

21 for three Re. Again for subcritical Re the cross-correlation decreased monotonically, while at $Re = 1.96 \times 10^5$ it displayed a periodic pattern as did the pressure cross-correlations of figure 18. These measurements were repeated with the cylinder shifted axially about one diameter, to ensure that the periodic pattern was not an artifact of the particular model surface condition.

4. Discussion

4.1. *Flow separation and reattachement*

While in steady flow the point of separation can be identified by the vanishing of the wall shear and the beginning of flow reversal; for unsteady boundary layers the definition requires further examination. Physically, separation should mark the termination of boundary-layer breakaway and the beginning of the region of flow reversal with considerable transverse dimensions and relatively low velocities. As Sears & Telionis (1975) have noted, the point of vanishing wall shear appears to have no special significance in unsteady flows. For example, an upstream moving separation exhibits a point of vanishing wall shear upstream of separation. Numerical boundary-layer solutions in unsteady flow have been successfully carried out through the point of vanishing wall shear, and Sears & Telionis have propsed to use the breakdown or loss of validity of the boundary-layer equations to signal the occurrence of separation. For oscillatory laminar boundary-layer flow, an empirical definition of the point of separation has been proposed by Despard & Miller (1971) as the farthest upstream point at which the wall shear is non-positive throughout the entire cycle of oscillation. Without dwelling on the complexities of the definition any further, it seems clear that instantaneous shear-stress and flow-direction data are necessary to define unsteady separation processes, which cannot be fully characterized by mean shear stress and mean velocity measurements alone.

As discussed in §3.3.2, the present fence probe measured the time-dependent flow direction, spatially-averaged across the fence height, and time-averaged across the vortex-shedding period. This averaging is expected to result (fortuitously) in a shift of the point of zero sensor differential pressure away from the point of zero skin friction and in the direction of the separation point. A more accurate determination of the position of separation as a function of time would require a more compact probe with better sensitivity, or more elaborate techniques which would indicate the instantaneous velocity profiles or vorticity at various angular positions, preferably simultaneously. For subcritical flow, the present probe showed intermittent flow reversals (see figure 14) shifted as expected a few degrees downstream from the separation-point data of Achenbach (1968), obtained using a mean shear stress probe consisting of a fence with a much smaller relative height. The separation point in this reference was defined as the location of zero mean shear stress. Dwyer & McCroskey (1973), using a surface film gauge and interpreting the abrupt change observed in the dynamic response of the gauge to indicate the passage of the separation point, measured separation-point excursions due to the vortex shedding from 75° to 85°, at $Re = 1.06 \times 10^5$. They also used a tandem-hot-wire probe placed within the cylinder boundary layer to identify a range between 75° and 90° where vortex shedding flow reversals occurred. These results are consistent with those shown in figure 14 for subcritical flow. The present results indicate also the presence in the subcritical range of low-frequency motions similar to those described by Sonneville (1976).

At the critical $Re = 1.96 \times 10^5$, the present data place the beginning of intermittent

reverse flow at about 87°. The probability, F_t, of downstream flow decreases first monotonically and sharply with increasing angle (see figure 14), becoming practically zero at $\theta \approx 89°$, and then increases to a local maximum at $\theta \approx 92°$. The presence of this maximum can be interpreted as an indication of intermittent flow reattachment. These data suggest a relatively fixed position (at about 89°) of the laminar separation–reattachment bubble when it manifests itself during the flow oscillations. Downstreatm of this angular location, say, at $\theta = 92°$, the flow is reversed when no reattachment occurs (subcritical flow conditions), and is in the downstream direction when the boundary layer reattaches and then separates again further downstream. At $\theta = 95°$, there is always reversed flow. The same observations were made on the opposite side of the cylinder, confirming the symmetry of the reattaching flow. The symmetry of the mean flow in the first region of the critical transition range had been also observed (with a different wind tunnel and cylinder model, without end plates) in an earlier investigation of Farell & Blessman (1983), in which no attempt was made to examine the time-dependent, spanwise flow structure.

On the basis of results of an oil-flow-visualization study, Dallman & Schewe (1987) have recently reported the appearance, at $Re = 1.85 \times 10^5$, of two well-defined, very straight separation lines on each side of a cylinder of aspect ratio 18, without end plates. While it is not clear how the presence of an oil film would affect the flow, Dallman & Schewe (also Son & Hanratty 1969) conjectured that the double-separation phenomenon is associated with the occurrence of small-scale laminar separation reattachment bubbles (and not with turbulent reattachment). This idea requires further verification and is not pursued here anymore.

4.2. *Vortex shedding*

Associated with the appearance in the critical range of intermittent flow reattachment, the large-timescale, large-amplitude variations in pressure and velocity described in §§3.2.2 and 3.2.3 (figures 10 and 11, spanwise location $z/D = 0.45$) were observed, associated with suppression of the regular shedding. The spectra of figure 8 show the deterioration of the shedding and the increase of low-frequency energy levels at critical Re that were a manifestation of these phenomena. The time dependent nature of the shedding is illustrated by the conditionally averaged spectra of figure 15 for the signal of figure 10 for $Re = 1.78 \times 10^5$. (In this figure, the ordinates have been normalized by the corresponding mean-square values.) The suppression of the vortex shedding for family C type segments reflects the spanwise non-uniform nature of the reattachment, to be discussed further in the next section. The low-frequency pressure and velocity variations were well correlated between them at any given spanwise position (see figure 9) and, as illustrated in figure 12, both were always symmetric and in phase.

4.3. *Possible effects of surface co..dition on the flow*

The high sensitivity of critical flow around a circular cylinder to minute protrusions on the cylinder surface has been highlighted in a recent paper by Schewe (1986). One should then examine whether the phenomena observed in the presnt paper could have been affected by the presence of the pressure taps, the fence probe or other surface irregularities. For the reasons stated below, the authors do not believe this to be the case.

First, measurements were obtained on two separate cylinders, with different sets of pressure taps, one mounted horizontally and the other one vertically. The latter cylinder allowed for variation of the aspect ratio. The same spanwise structures were

observed in all cases. The aspect ratios were moderate, and end plates were used to reduce end effects.

On model A, there was no fence probe. The model was shifted axially, and the cross-correlations between wake velocities, and also between surface pressure fluctuations, were measured. The results showed no effect of the presence of the presssure taps nor of other surface roughnesses. Note that the protrusion in Schewe's experiment affected the flow on the side of the cylinder having the protrusion and made the global flow pattern asymmetric. In the present experiment, measurements of circumferential pressure cross-correlations, and of velocity cross-correlations, between opposite sides of the cylinder, demonstrated that the mean flow was symmetric. These results are not shown for brevity and because similar results are shown for model B.

On model B, the spanwise mean pressure distributions in figures 5–7 were measured prior to installation of the fence probe. The results show the spanwise structures linked to the boundary-layer oscillations, as discussed in the next section. The fence probe was subsequently installed to study the details of the flow fluctuations. The spanwise pressure cross-correlations in figure 18 were thus measured after the fence probe was installed. The results agree with the cross-correlations measured behind model A without a fence probe. Furthermore, the cross-correlations between opposite sides of the cylinder in figure 12 indicate that the low-frequency flow motions were symmetrical between the side with the fence and the opposite side without the fence.

4.4. *Spanwise characteristics of the flow*

At critical Re, the large-amplitude, low-frequency flow components were identified with the intermittent flow reattachment occurring simultaneously on both sides of the cylinder. The strong negative correlations between the large-amplitude pressure fluctuations at two spanwise locations (figures 16, 17*b*) indicated that these low-frequency motions were produced with a definite periodicity in the spanwise direction. The spanwise variation of the time-averaged pressure correlation in figure 18 shows that the boundary-layer motions take place in a segmented manner and become out of phase at a moderate spacing. The low-frequency boundary-layer oscillations produced a corresponding movement of the wake, as the coherence pattern in figure 9 demonstrated, and the cross-correlation between the low-pass filtered velocity fluctuations in the wake exhibited the same spanwise structure. As can be seen in figure 21, while the boundary-layer motions are in phase in the spanwise direction at subcritical Re, at critical Re the wake motions associated with the intermittent flow reattachment occurred with neighbouring cells oscillating out of phase with each other. The overall reduction in vortex shedding intensity (and virtual suppression for family C type segments) at critical Re reflect both the spanwise non-uniformity and intermittent reattachment of the flow.

The flow oscillations at critical Re, in turn, result in the non-uniform spanwise mean pressure contours shown in figures 6 and 7. During flow reattachment, the level of the surface pressure decreases momentarily, with the end result that a low value of the time-averaged pressure is produced in the region where the flow movement is the largest. The spanwise regions with the low values of the cross-correlation correspond to the nodes of the oscillation and less negative mean pressures. The relatively uniform base pressure distributions (see also figure 4) are characteristic of the separated shear layer. The spanwise structures were observed on both model A ($AR = 5$) and model B ($AR = 5, 8$), and were independent of the particular model

surface condition. A definite conclusion regarding cell size was not possible from the present data. While for model B the cell size (obtained from the pressure correlations) appeared to be independent of the aspect ratio, the cell size for model A with an aspect ratio of 5 and slightly larger diameter (obtained from wake velocity correlations) was smaller.

Several indications of spanwise three-dimensional structures in nominally two-dimensional flows around cylinders can be found in the literature. Using long silk threads attached at the stagnation point for flow visualization, Humphreys (1960) found a stable spanwise cell pattern, formed of cells with and without reattachment, at $Re = 10^5$. The cell size was approximately 1.4 to 1.7 cylinder diameters, independent of the diameter. The threads apparently organized the flow, tripping the cross flow from laminar to turbulent separation regions. Humphreys advanced the idea that the same type of cell formation could exist at the lower edge of the critical range, even if the threads were removed, without any well-defined periodicity, but rather with the cells of turbulence moving about randomly on the cylinder surface. Korotkin (1976), on the other hand, found regular and significant mean pressure non-uniformities at $Re \approx 10^6$, along cylinder generatrices just before and in the zone of separation, not generally reported in the literature at such large Re. Using silk threads as well, Korotkin found the same type of cell structures as Humphreys at this Re, and also at a subcritical $Re = 5 \times 10^4$. Sonneville's (1976) pressure and velocity measurements at $Re = 4.5 \times 10^4$, however, did not disclose any spanwise non-stationary behaviour; statistically, the flow was two-dimensional, and no phase differences were detected in the mean along the cylinder span.

Spanwise structures with a cell length of about two cylinder diameters, at a super critical $Re = 4.1 \times 10^5$, have been recently observed by Dallman & Schewe (1987) using an oil-flow-visualization technique. It is not clear how the presence of the oil film would affect the relevant instability phenomena. The spanwise cells were not present at $Re = 1.85 \times 10^5$ and instead, spanwise uniform, twin neighbouring separation lines were observed at this Re, as discussed earlier, on each side of the cylinder. The present results, on the other hand, at Re somewhat smaller than 2×10^5, did show two closely spaced points on separation but with a superimposed spanwise cell structure. (The difficulty of comparing corresponding Reynolds numbers in different experiments should be borne in mind.) The cell pattern observed in the present result was not an artifact of the cylinder surface condition, nor was it caused by the incoming free-stream conditions (see §4.3).

Korotkin suggested that his observed cell structure could be related to the concavity of the streamline near separation. To the authors' knowledge, this assumption has not been substantiated. Boundary-layer transitional lambda vortex structures, on the other hand, are typically several boundary-layer displacement thicknesses wide (see e.g. Perry, Lim & Teh 1981) and are too small for the spanwise cell pattern presently observed. Wei & Smith (1986) found also small, cell-like secondary vortex structures in the free shear layers of a cylinder, at relatively low Reynolds numbers. It is doubtful that these small-scale free-shear-layer structures, even if they persist at much higher Reynolds numbers, may develop into the three-dimensional cells presently observed, in particular because an increase in Re should result in even smaller spanwise cells with correspondingly narrower spacing. One could perhaps conjecture (as suggested by Dallman & Schewe for their supercritical flow-visualization results) that the cell structures seen in the present results are related to a global instability of the wake region, giving rise to cells basically dependent on cylinder diameter. It is noteworthy that the boundary-layer

oscillations associated with the present structures were symmetric on both sides of the cylinder while being out of phase between neighbouring cells. Though the origin of these segmented, symmetric motions of the boundary layer remains to be investigated, the present study has shown that the reduction in vortex shedding intensity and in drag coefficient which occurs at the beginning of the critical range is due to intermittent, spanwise non-uniform flow reattachment, with final separation occurring a few degrees downstream of the position of initial separation, itself realtively fixed in angular location.

5. Conclusions

The flow around smooth circular cylinders at the beginning of the critical transition was experimentally investigated over the range $1.5 \times 10^5 < Re < 2 \times 10^5$, where the C_d decreases from a subcritical value of about 1.15 to about 0.9, and was compared with flow at subcritical Re. The shedding intensity decreased markedly as Re increased beyond about 1.5×10^5. This decrease was accompanied by a broadening of the peaks and by a shift in energy toward low-frequency components. The pressure– and velocity– time traces exhibited large-timescale fluctuations associated with suppression of the regular vortex shedding. These low-frequency flow components involved surface pressure excursions toward more negative values, which were well-correlated with large wake-velocity fluctuations.

In addition to velocity and pressure fluctuation measurements, the time-dependent flow direction was measured on the cylinder surface near the separation and reattachment points. Intermittent boundary-layer reattachments were found to occur at critical Re symmetrically on both sides of the cylinder, forming spanwise cell-like structures with well-defined periodicity. Though other indications of spanwise three-dimensional structures in nominally two-dimensional flows around cylinders at various Reynolds numbers can be found in the literature, the origin of these segmented, symmetric boundary-layer motions requires additional investigation. The present structures were observed with different end conditions and aspect ratios, and were independent of cylinder orientation in the tunnel. The associated wake motions occurred with neighbouring cells oscillating out of phase with each other. The position of the laminar separation–reattachment bubble was relatively fixed (at about 89°), with final separation after the intermittent reattachment occurring a few degrees downstream. The intermittent, non-uniform reattachment of the flow results in the observed reductions in vortex shedding intensity and drag coefficient which occur at the beginning of the critical range.

This work was conducted by the authors at the Department of Aerospace Engineering and Mechanics, University of Minnesota. C.F. acknowledges partial support from the National Science Foundation under Grants NSF/INT808014 and ENG78-22092.

REFERENCES

ACHENBACH, E. 1968 Distribution of local pressure and skin friction around a circular cylinder in cross-flow up to $Re = 5 \times 10^6$. *J. Fluid Mech.* **34**, 625–639.

ALLEN, M. J. & VINCENTI, W. G. 1944 Wall interference in a two-dimensional-flow wind tunnel with consideration of the effect of compressibility. *NACA Tech. Rep.*

ALMOSNINO, D. & MCALISTER, K. W. 1984 Water-tunnel study of transition flow around circular cylinders. *NASA Tech. Mem.* 85879.

BEARMAN, P. W. 1969 On vortex shedding from a circular cylinder in the critical Reynolds number region. *J. Fluid Mech.* **37**, 577–585.

DALLMAN, U. & SCHEWE, G. 1987 On topological changes of separating flow structures of transition Reynolds numbers. *AIAA*–87–1266.

DESPARD, R. A. & MILLER, J. A. 1971 Separation in oscillating boundary layer flows. *J. Fluid Mech.* **47**, 21–31.

DWYER, H. A. & MCCROSKEY, W. J. 1973 Oscillating flow over a cylinder at large Reynolds number. *J. Fluid Mech.* **61**, 753–767.

FARELL, C. & BLESSMAN, J. 1983 On critical flow around smooth circular cylinders. *J. Fluid Mech.* **136**, 375–401.

FARELL, C. & FEDENIUK, S. 1987 Effect of end plates on the flow around rough cylinders. *7th Int Conf. on Wind Engineering, Aachen, West Germany*, pp. 87–98.

GÜVEN, O., FARELL, C. & PATEL, V. C. 1980 Surface roughness effects on the mean flow past circular cylinders. *J. Fluid Mech.* **98**, 673–701.

HIGUCHI, H. 1985 A miniature directional surface-fence gage. *AIAA J.* **23**, 1195–1196.

HUMPHREYS, J. S. 1960 On a circular cylinder in a steady wind at transition Reynolds numbers. *J. Fluid Mech.* **9**, 603–612.

KIM, H. 1986 An experimental investigation on the flow around a circular cylinder in the first critical subregion. PhD thesis, University of Minnesota.

KOROTKIN, A. I. 1976 The three-dimensionality of the flow transverse to a circular cylinder. *Fluid Mechanics-Soviet Research*, **5** (2), 96–103.

PERRY, A. E., LIM, T. T. & TEH, E. W. 1981 A visual study of turbulent spots. *J. Fluid Mech* **104**, 387–405.

SCHEWE, G. 1983 On the force fluctuations acting on a circular cylinder in crossflow from subcritical up to transcritical Reynolds number. *J. Fluid Mech.* **133**, 265–285.

SCHEWE, G. 1986 Sensitivity of transition phenomena to small pertubations in flow around a circular cylinder. *J. Fluid Mech.* **173**, 33–46.

SEARS, W. R. & TELIONIS, D. P. 1975 Boundary-layer separation in unsteady flow. *SIAM J. Appl. Maths* **28**, 215–235.

SON, J. S. & HANRATTY, T. J. 1969 Velocity gradients at the wall for flow around a cylinder at Reynolds numbers from 5×10^3 to 10^5. *J. Fluid Mech.* **35**, 353–368.

SONNEVILLE, P. 1976 Étude de la structure tridimensionnelle des écoulements autour d'un cylindre circulaire. *Bull. Direction des Etudes et Recherches Electricité de France*, Ser. A, no. 3.

WEI, T. & SMITH, C. R. 1986 Secondary vortices in the wake of circular cylinders. *J. Fluid Mech.* **169**, 513–533.